Aerodynamic Heating of a Cylinder between Flat Plates

Layton W. Howerton*, Gregory A. Blaisdell†, and Jonathan Poggie‡
Purdue University, West Lafayette, Indiana 47907

Reynolds-averaged Navier-Stokes (RANS) calculations and improved delayed detached eddy simulations (IDDES) are applied to a cylinder located between flat plates in Mach number 5.95 flow. The cylinder diameter is on the order of twice the gap between the flat plates for the initial configuration. The geometry is a simplified representation of the torque tube in a missile-fin configuration. Experimental results from wind tunnel tests collected in 1979 at the Arnold Engineering Development Center are used for comparison. Previous RANS simulations of the experimental setup are also used for comparison. The heat flux, pressure, and skin friction are calculated and compared. The unsteady shock-wave/boundary-layer interactions due to the presence of the cylinder are evaluated with IDDES methods. Areas of high heat transfer are identified and compared to experimental data. Computationally identifying the locations of high aerothermodynamic loading may provide useful information when designing thermal protection systems for future aerospace vehicles.

Nomenclature

C_f	=	skin friction coefficient
CFL	=	Courant-Friedrichs-Lewy number
D	=	cylinder diameter
f_s	=	sampling frequency
$G(f)$	=	power spectral density
g_h	=	gap height
h	=	heat transfer coefficient
M	=	Mach number
P	=	pressure
$\dot{q}$	=	heat flux
Re	=	Reynolds number
S_t	=	Strouhal number
T	=	temperature
t	=	time
Δs	=	first cell wall-normal grid spacing
$\Delta(x, y, z)^+$	=	nondimensional coordinates in viscous wall units
ν	=	kinematic viscosity
τ	=	shear stress
$()_{ref}$	=	reference property
$()_w$	=	wall property
$()_\infty$	=	freestream property
$()_0$	=	stagnation property

I. Introduction

Geometric imperfections, such as gaps and cavities, on aerospace vehicles have the potential to have disastrous consequences in high-speed flight if the thermal protection system is inadequate. The complex flows which can develop on these common geometries can significantly change the aerothermodynamic loading compared to that which occurs in

---

*Graduate Student, School of Aeronautics and Astronautics, AIAA Student Member.
†Professor, School of Aeronautics and Astronautics, AIAA Associate Fellow.
‡Professor, School of Aeronautics and Astronautics, AIAA Associate Fellow.

flow over a nominal outer mold line of the vehicle. Extant research shows that gaps and cavities experience high heating [1, 2]. The present work aims to further the body of research into gap flows. Heat flux, pressure, and skin friction will be of particular interest for characterizing aerothermodynamic loading and shock-wave/boundary-layer interaction. Aerothermodynamic loading is the result of the heat transferred between air and body and the pressure acting on the body. Shock-wave/boundary-layer interactions can cause the boundary layer to separate, and skin friction will help determine these separation events. Shock-wave/boundary-layer interactions also present well-studied unsteady behavior [3, 4].

The configuration selected to be evaluated represents a simplification of the experimental setup of Neumann [5] as well as the recent RANS computations of Alviani et al. [6]. A cylinder with a flat plate above and below represents a post which could attach a fin to a missile. One of the flat plates represents the missile body, and the other flat plate represents the bottom face of the missile control fin. With this simplification, some differences to a full missile-fin-post configuration include the potential curvature of the missile body, the potential curvature of the bottom face of the control fin, the limited spanwise extent of the fin surface, which can affect the three-dimensional structure of the flow; and the shock-wave/boundary-layer interaction between the fin leading edge shock and boundary layer which developed on the missile body upstream. In Fig 1, the top and bottom plates are shown in gray, the cylinder is shown in red, the inflow is the $-x$ face in blue and the outflow is the $+x$ face. The cylinder diameter is $D = 15.9$ mm, and the gap, $g_h = 7.62$ mm between the upper and lower plate, was one previously studied [5] [6]. The cylinder diameter will be used throughout for nondimensionalzation.

The outline of the paper is as follows. Section I provides an introduction and motivation for the research. Section II describes the methodology used to simulate the desired conditions. Section III examines the computational results. Section IV summarizes and concludes the discussion.
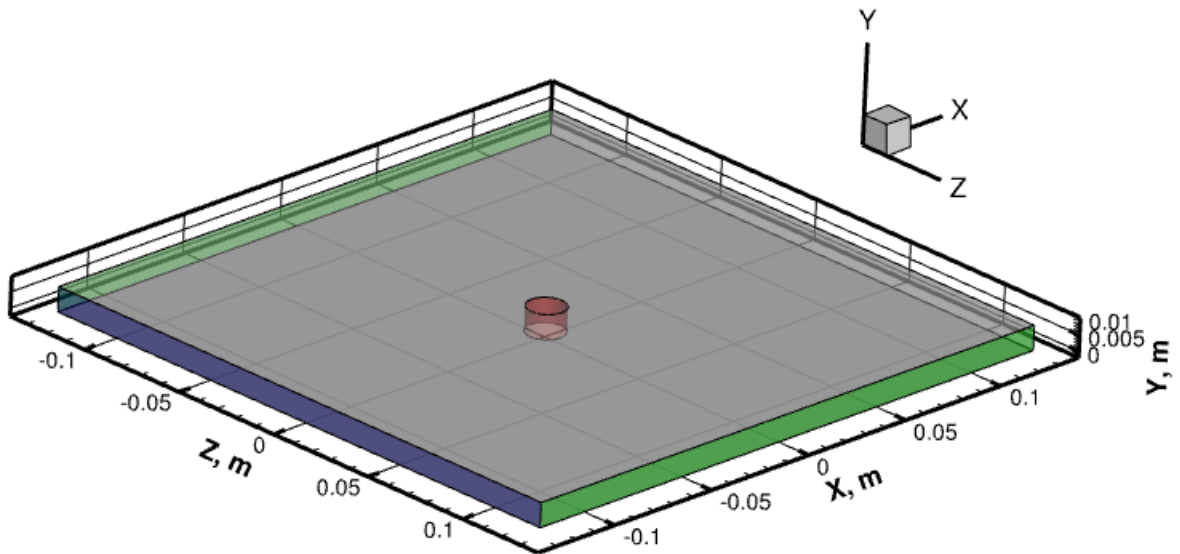

Fig. 1   Computational domain.

II. Methodology

Freestream conditions are listed in Table 1. Computational grids were created in the commercial grid software Pointwise. Post-processing computational data was completed with Tecplot and MATLAB software. CREATE-AV Kestrel is the Department of Defense computational fluid dynamics package used for the present work. The Kestrel computational fluid dynamics (KCFD) solver is the portion of the software package used for the simulations discussed. KCFD uses a finite-volume, unstructured, cell-centered approach. When computing inviscid fluxes, the Harten-Lax-van Leer-Einfeldt (HLLE++) method was employed. The viscous flux scheme used was the alpha-damping method. Van Leer's scheme was used for the calculation of convective flux Jacobians. Kestrel has a flux limiter called Kestrel+ which was used. The simulations were run using second-order accuracy spatially and temporally. The second-order

accuracy in time relied on a subiterative point-implicit scheme [7]. Three subiterations were completed during each iteration. The Splart-Allmaras (SA) turbulence model has been used for the simulations. For the RANS calculations, the CFL number has been left at the default value of 1000 for KCFD. KCFD was then used in the improved delayed detached eddy simulation (IDDES) mode to investigate unsteady motion in the shock-wave/boundary-layer interaction. The wall boundary condition used for both plates and the cylinder was isothermal no-slip surface at T_w = 300 K. The inlet condition was set to freestream conditions. The outflow boundary coundition was extrapolated. The spanwise boundary conditions were symmetry. For the IDDES runs, the time step used was $\Delta t = 1 \times 10^{-7}$ s. The simulation was sampled at several frequencies. Time histories at points of interest were sampled at f_s = 10 MHz which corresponds to every computational time step. Planar cuts along the centerline upstream of the cylinder and all model surfaces were sampled at f_s = 10 kHz. Full volume solutions were collected at f_s = 1 kHz. Slightly more than 225,000 iterations were completed for this simulations which corresponds to 22.5 ms of physical time. Time-averaging was started after transients were allowed to pass. Simulation start-up transients were monitored with moving averages of parameters of interest. The moving averages asymptote toward the time-averaged value, and this was used for transient cut off. Computational resources for these simulations were provided by the Navy DoD Supercomputing Resource Center HPE Cray EX system, Narwhal. Narwhal uses AMD Epyc ROME 7H12 processors which are clocked at 2.6 GHz. Each Narwhal node has two 64-core processors, and 50 Narwhal nodes were used for these computations.

Table 1   Freestream flow conditions

Parameter	Value
M_∞	5.95
ρ_∞	0.07017 kg/m^3
P_∞	1149 Pa
T_∞	57.06 K
μ_∞	3.753×10^{-6} Pa $\cdot$ s
u_∞	900.9 m/s
$P_{0\infty}$	1.724×10^6 Pa
$T_{0\infty}$	461.1 K
Re_∞	1.685×10^7 m^{-1}

A. Computational Mesh

The grid generation was completed with the commercial grid generation software, Pointwise. All grids created are fully structured grids. For the RANS simulations, a coarse, medium, and fine grid were used for grid independence studies. Iterative convergence was also examined and will be discussed in Section III. The coarse grid has an initial wall spacing Δs of 6×10^{-6} m and contains approximately 607,000 points. The medium grid has a Δs of 3×10^{-6} m and contains approximately 3.48 million points. The fine grid has a Δs of 1.5×10^{-6} m and contains approximately 21.2 million points. Each grid has a nondimensional distance from the wall, $\Delta y_w^+ \leq 1$ in the portions of the domain with attached boundary layer. The grid has a circular region of radially aligned cells that are then smoothed with an outer region with the Steger-Sorenson boundary control function implemented in Pointwise. The outer regions are normal to the exterior boundary conditions. The smoothing removes sharp corners from the grid and lowers the maximum included angle found in the domain. The coordinate system for the grid is centered at the center of the cylinder on what will be described as the bottom, y = 0 wall. The x,y, and z directions correspond to streamwise, wall-normal, and spanwise directions. The dimensions of the computational domain were: -0.1272 m< x <0.1272 m, 0m< y <0.00762 m, and -0.1272 m< z <0.1272 m.

For the IDDES grids, several iterations of the grid were prepared, and preliminary calculations were performed to estimate the nondimensionalized grid coordinates. These provided some sense of the final nondimensionalization and informed grid spacings. The grid consists of a inner LES quality grid stemming radially from the cylinder which is then smoothed into a more RANS quality grid. The smoothing was again implemented in Pointwise with the Steger-Sorensen boundary control function. The grid density difference between these two regions can be seen qualitatively in Fig. 2 (b). The RANS portion of the grid was slightly higher wall resolution than the fine RANS simulation at Δs of 1×10^{-6} m. The LES to RANS quality grid was selected to be at x/D = 5 because it was desired to keep the initial separation

location in the LES quality region. The attached boundary layer in the RANS quality grid maintained $\Delta y_w^+ \leq 1$. The inner coordinates in the LES quality region are $\Delta x^+ \approx 40$, $\Delta z^+ \approx 23$, and $\Delta y_w^+ \leq 1$. In the LES region, the cells are kept as cubic as possible away from the walls. A value of $\Delta y^+ \approx 4$ is achieved in the LES quality regions away from the walls. The values align well with and were targeted for the grid resolution ranges recommended for wall-solved LES [8]. Centerline values of nondimensionalized time step $(\Delta t^+ = (\tau_w/\rho_w)\Delta t/\nu_w)$ and Δy_w^+ are shown in Fig. 3. The spikes in Fig. 3 near the cylinder occur in a region of separated flow and were neglected when evaluating the attached boundary layer Δy_w^+ values. The mesh contains 221.9 million cells, of which 203 million are located in the LES quality region.

(a) $z = 0$ plane   (b) $y = 0$ plane
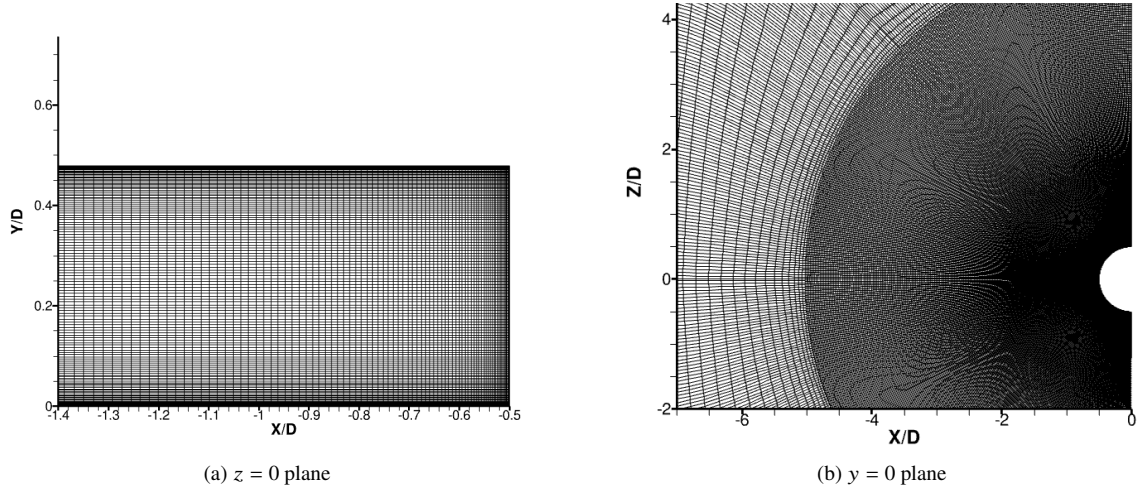
Fig. 2   IDDES Computational grid in SWBLI region. Every other grid point plotted for clarity.
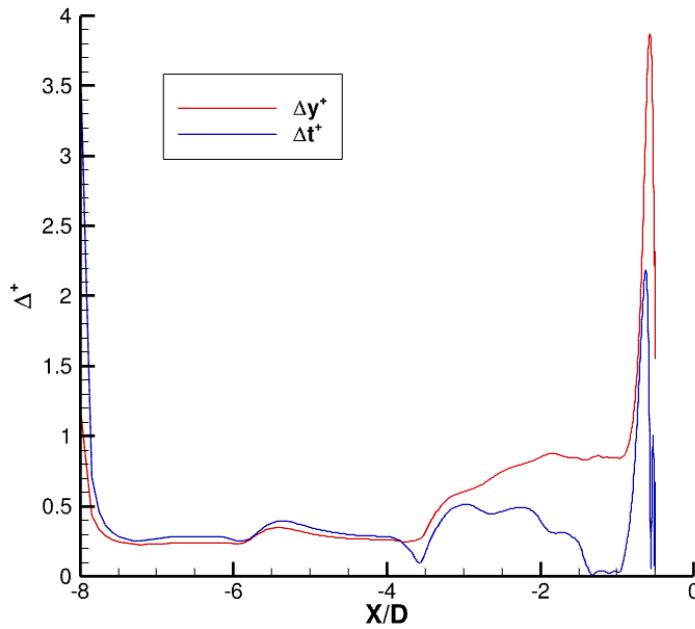
Fig. 3   IDDES nondimensionalized wall normal grid spacing and time step along top plate centerline ($z = 0$).

III. Results

The primary focus of this work was to evaluate and compare the IDDES and RANS simulations and provide a steping stone simulation in a build up to time-accurate simulations of missile-fin interaction regions. The current configuration has some sizable assumptions and simplifications that make extensive quantitative comparison to the experiment carried out by Neumann and Hayes [5] as well as previous RANS calculations [6] not ideal. However the data trends will be compared. The unsteady simulation has no experimental or simulation data to compare to directly, but trends can be compared to other flows studied in the literature. Shock-wave/boundary layer interactions studies have shown unsteadiness to be an important aspect of high-speed flows. The low frequency component to the unsteadiness present in the shock-wave/boundary layer interaction has been the subject of many studies [3, 4, 9]. The results described here will look at both the unsteady and time-averaged results from the IDDES as well as the steady RANS solutions. Wall pressure, skin friction coefficient and heat transfer coefficient will be the primary focus. Density gradient magnitude will be used to show the unsteady large-scale movement of the separated region. Power spectral density plots will be used to evaluate frequency content at specific locations in the flow.

For time-averaged and fluctuating quantities the results, the following forms were used, where N is the total number of timesteps, $t = n\Delta t$, and $\psi(t)$ is the time history of a quantity of interest,

$$\bar{\psi} = \frac{1}{N} \sum_{N=0}^{N-1} \psi(n\Delta t) \tag{1}$$

$$\psi'(t) = \psi(t) - \bar{\psi} \tag{2}$$

A. RANS Results

Coarse, medium, and fine grids were evaluated for iterative and grid convergence with streamwise skin friction coefficient, surface pressure, and heat transfer coefficient in Figs. 4, 5, and 6. The heat transfer coefficient [10] is defined here as

$$h = \frac{\dot{q}_w}{0.9T_{0\infty} - T_w} \tag{3}$$

with $\dot{q}_w$ as wall heat flux per unit area in W/m^2, T_w as wall temperature in K, and $0.9T_{0\infty}$ being a reference value in K. This reference was chosen for consistency with previous studies [5] [6]. For iterative convergence, plots are taken from several iteration counts and plotted together. For the demonstration of grid convergence, the coarse, medium, and fine grids are plotted together. The flow has an attached boundary layer which develops from zero thickness at the inflow plane. The boundary layer along the top wall separates on the centerline at $x/D = -2.55$ as indicated by the streamwise skin friction coefficient becoming negative. At the same streamwise location, there is an accompanying increase in wall pressure and heat transfer coefficient. Iterative and grid resolution convergence is demonstrated. In the attached boundary layer upstream of separation, the grid level of medium to fine and coarse grid iteration from 50,000 to 100,000 changed the solution by less than 3%. The RANS results shown correspond to the fine mesh unless otherwise noted.

The streamwise skin friction coefficient taken from the centerline upstream of the cylinder on the top wall is shown in Fig. 4. The skin friction coefficient is high at the start inflow to the domain as the freestream conditions meet the no-slip walls. There is a relatively constant value of C_{fx} from $x/D = -7$ to $x/D = -3$. This portion of the domain has an attached boundary layer. The variations that can be seen such as at approximately $X/D = -5.5$ are likely due to the train of oblique shocks which emanate from the initial inflow boundary layer growth. The boundary layer separates at $x/D = -2.55$ and reattaches at $x/D = -0.59$. At $x/D = -0.52$ the flow separates a second time before reaching the cylinder. In Fig. 5 and Fig. 6 the dominant feature is the peak which occurs at reattachment. In the RANS simulations of Alviani et al. [6] the peak normalized pressure on the separating wall for the simulation with the same gap height to cylinder diameter ratio as that used here and no freestream angle of attack was $P_w/P_\infty = 9$. The simulations of Alviani et al. included the entire missile geometry and the gap was smaller than the boundary layer thickness at the start of the gap region. The Mach number reduction due to ingesting the lower portion of a boundary layer into the gap also affects the maximum heating. In Alviani et al. the peak heat transfer coefficient for the associated simulation was on the order of $h/h_{ref} = 20$. The peak in Fig. 6 is roughly $h/h_{ref} = 85$. The highest heat transfer coefficient seen in the experimental data of Neumann and Hayes [5] was $h/h_{ref} = 7$. The closest point to the cylinder measured by Neumann and Hayes on Fig. 6 was at $x/D = -0.8$. At $x/D = -0.8$ the RANS produced a $h/h_{ref} = 9.9$. However, closer to the cylinder at $x/D = -0.52$ on Fig. 6 the RANS fine grid solution is $h/h_{ref} = 81$. This indicates the nearest experimental

point to the cylinder was not close enough to capture peak heating. This assessment agrees with the findings of Alviani et al. Additionally, no heat transfer data was collected experimentally on the cylinder itself. However, Fig. 7 and the simulations of Alviani et al. found the peak heating globally to consistently be located on the cylinder at the point of reattachment. The trends in Fig. 4, 5, and 6 are similar to other supersonic blunt bodies attached to plates [11].
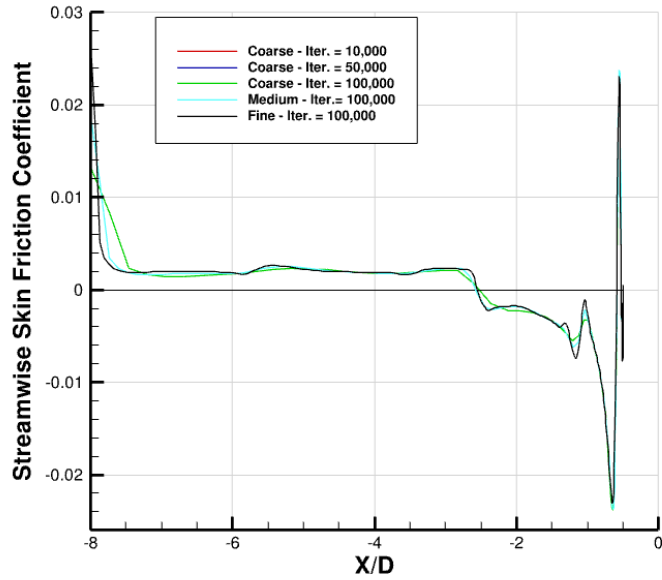

Fig. 4   RANS C_{fx} **Streamwise skin friction coefficient centerline top plate, including iterative and grid convergence.**
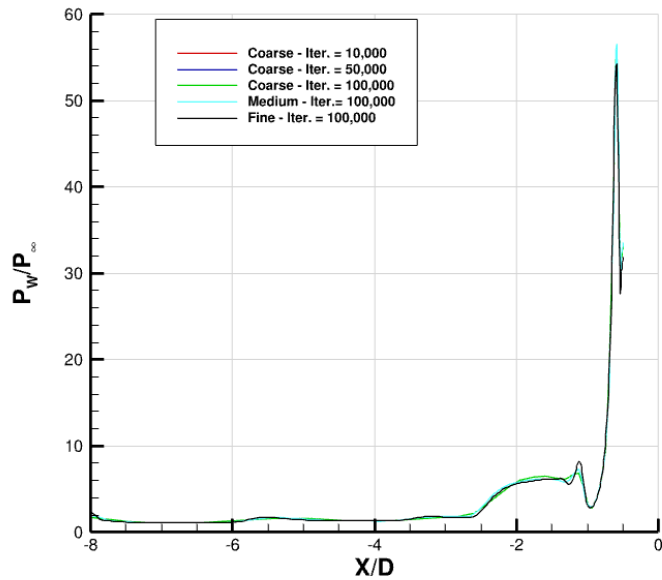
Fig. 5   RANS pressure centerline top plate, including iterative and grid convergence.
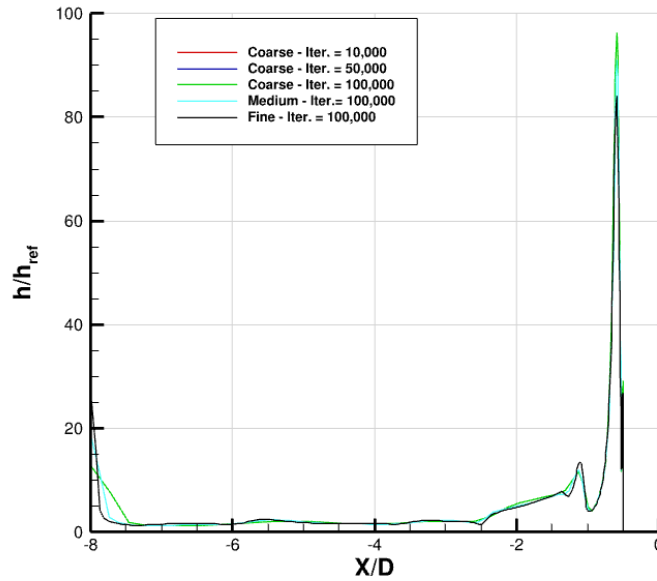
Fig. 6 RANS heat transfer coefficient centerline top, including iterative and grid convergence.
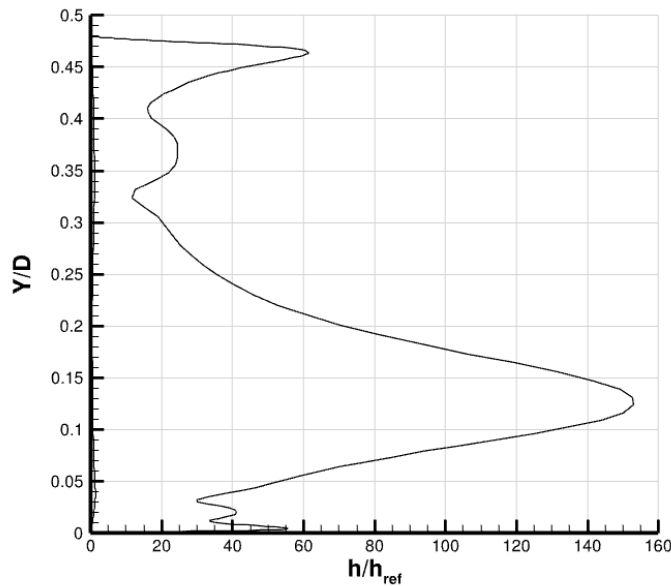
Fig. 7 RANS heat transfer coefficient on cylinder leading edge.

Figure 8 shows the RANS Mach number contour on the $z = 0$ centerplane. Upstream of the separation, the reflecting oblique shocks can be seen. The separation at $x/D = -2.55$ can be seen with the low-Mach number region on the upper wall. Then at the cylinder interaction region, the flow display some elements which are similar to those seen in blunt fin interactions. The separation shock on a blunt fin normally has an interaction with the bow shock from the blunt fin, but here the gap height limits that interaction. The initial separation shock from the top wall interacts with the bottom wall causing that wall to separate at $x/D = -1.63$ as seen in Fig. 9 and Fig. 10. The bottom wall reattaches

before separating again in a corner vortex at the intersection of the plate and cylinder. Figure 11 shows the peak pressure occurs near the corner vortex between the bottom wall and the cylinder. The increase in static pressure can also be seen across the separation shock. Peak pressure on the cylinder leading edge normalized by freestream static pressure is $P_w/P_\infty = 133$ as seen in Fig. 12. Along with Fig. 7, this indicates the location on the cylinder face which the shock impinges is roughly $y/D = 0.13$. The streamlines in Fig. 9 approaching the corner vortex are directed up and into the cylinder face at that location. The streamlines show qualitatively the reattachment location just discussed with the associated pressure and heat transfer rise.
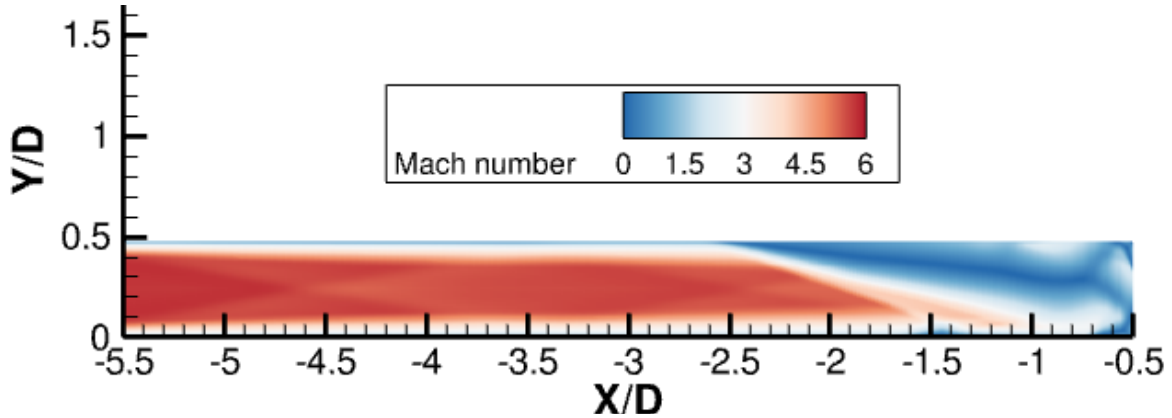
Fig. 8   Centerline plane RANS Mach number.
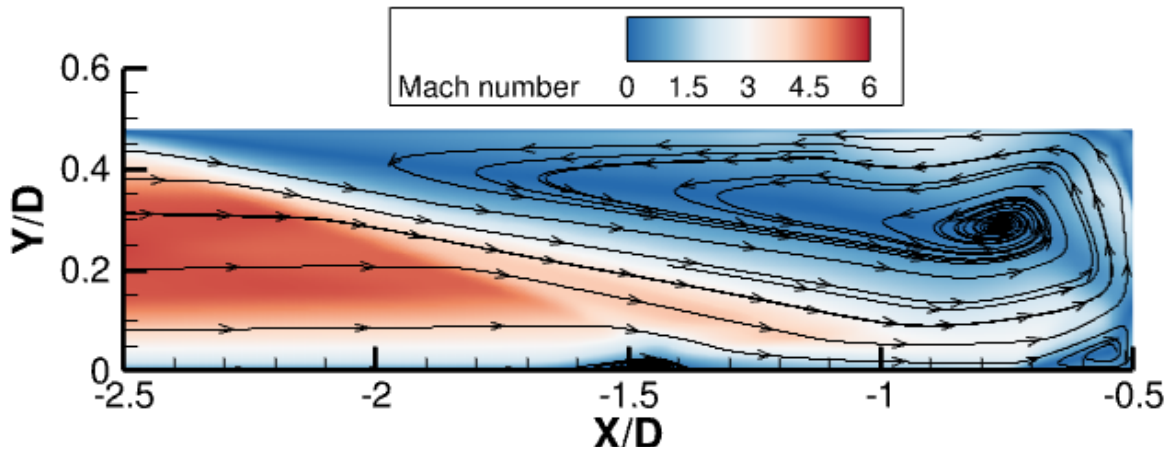
Fig. 9   Centerline plane RANS Mach number, including velocity streamlines.
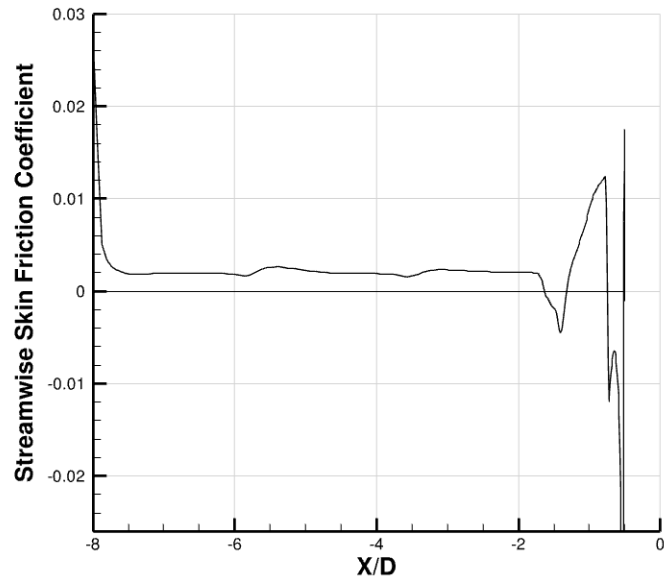
Fig. 10 RANS C_{fx} Streamwise skin friction coefficient centerline bottom plate, fine grid.
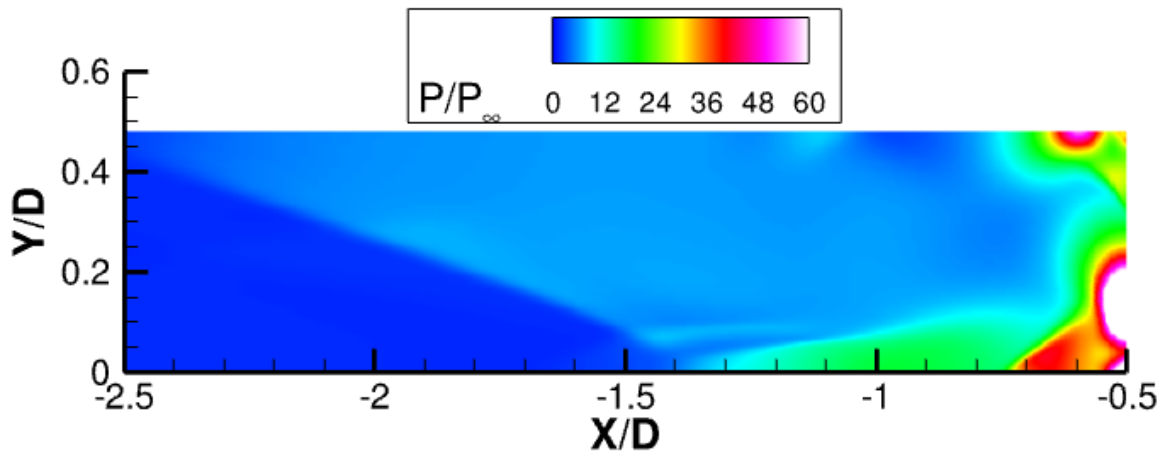
Fig. 11   Centerline plane RANS pressure.
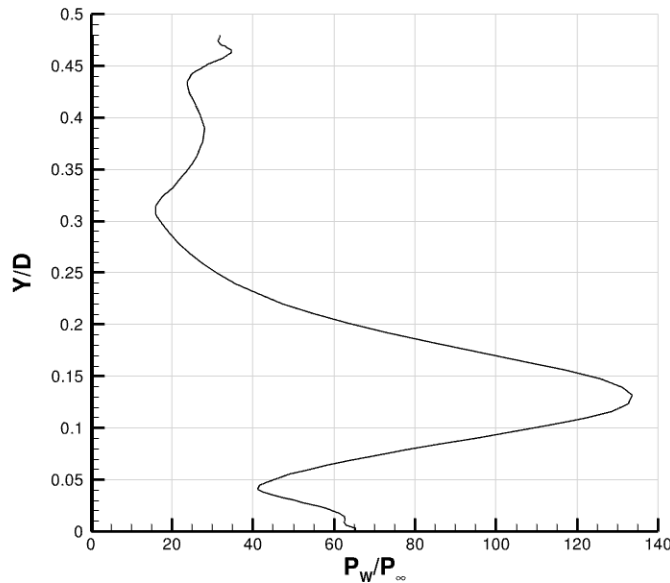
Fig. 12   RANS pressure cylinder leading edge.

B. IDDES Results

The dominant feature of the IDDES simulation is the large amplitude motion of the leading separation moving in the streamwise direction. This behavior will be discussed in more detail later in this section. Figure 13 shows the time-averaged IDDES skin friction coeffiecient on the top and bottom walls. Comparing to Fig. 4 and Fig. 10, the time-averaged IDDES initial separation occurs significantly further upstream. There is over a full cylinder diameter difference between the values. The time-averaged IDDES initial separation location is at $x/D = -3.6$ compared to the separation of the RANS at $x/D = -2.55$. Interestingly the bottom wall separates, as determined by negative streamwise skin friction coefficient, closer to the cylinder compared to the RANS solution. The RANS bottom wall separates at $x/D = -1.63$ while the time-averaged IDDES bottom wall separates at $x/D = -1.31$. The bottom wall in the RANS reattaches before separating again near the corner, but the time-averaged IDDES separates and does not follow that behavior. The bottom wall remains separated and the vortex at the intersection of the bottom wall and cylinder face is much larger as can be seen with the streamlines in Fig. 14. Fig. 15 has higher peak wall pressure values compared to the RANS solution. The RMS of pressure fluctuations in Fig. 16 show relatively constant values on the top wall until approximately $x/D = -1.5$. Downstream of $x/D = -1.5$, the RMS of wall pressure fluctuations increases dramatically. The locations where the RMS of pressure fluctuations are zero were solved using the RANS formulation portion of IDDES. The IDDES solution saw higher peak values of heat transfer coeffiecient on the top plate shown in Fig. 17 compared to the RANS solution. The peak heat transfer coefficient on the cylinder face, Fig. 18, is of approximately the same magnitude as the on the top plate. Comparing the peak values the of roughly $h/h_{ref} = 130$ and $h/h_{ref} = 95$ for RANS and IDDES respectively, shows the importance of heating on the cylinder. Agreeing with the findings of Alviani et al., the global peak heat transfer coefficient was likely not found in the experiments because no heat transfer data were taken on the cylinder face. The location of the maximum heat transfer coeffiecient on the cylinder is at a much higher y/D location in the IDDES, and the reason can be see qualitatively from comparing the flow structure in Fig. 9 and Fig. 14. The size of the corner vortex at the bottom wall intersection with the cylinder dictates the location where the flow reattaches, and the reattachment then produces the high heat transfer.
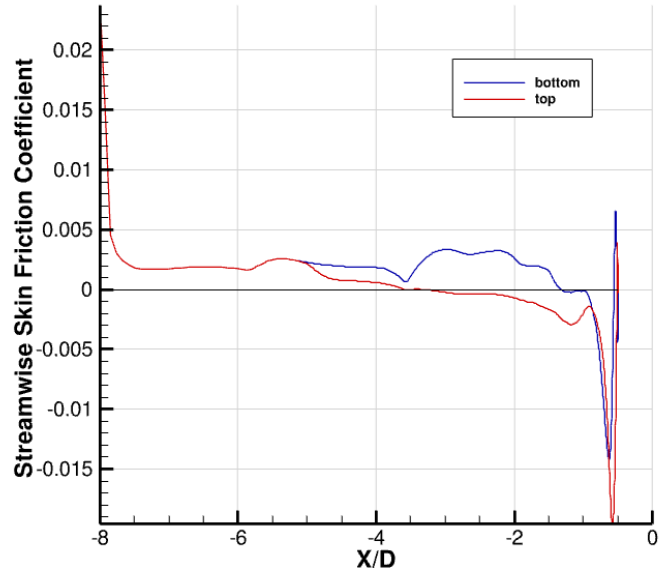
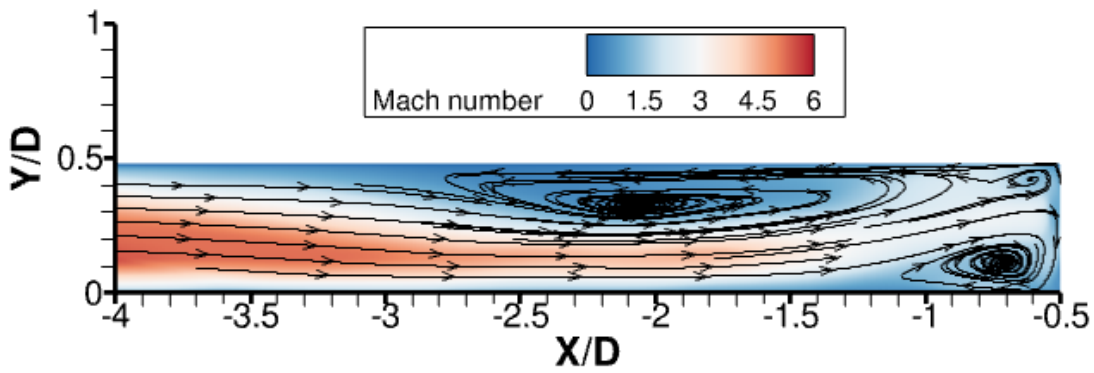**Fig. 13 IDDES C_{fx} time-averaged streamwise skin friction coefficient centerline top and bottom plate.**

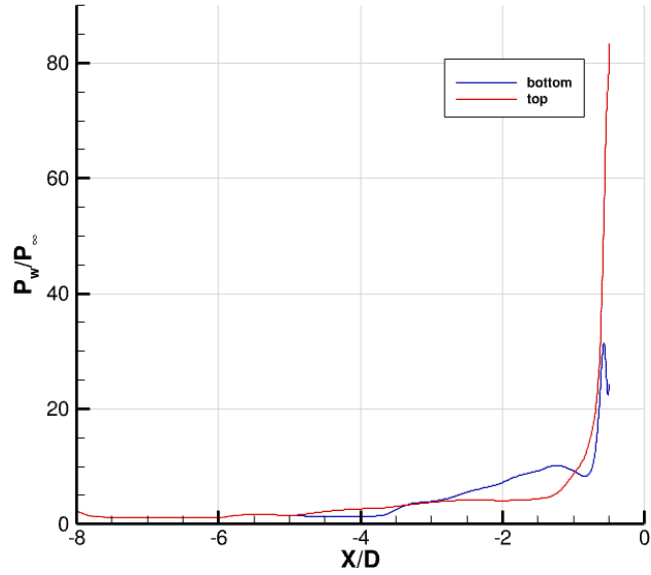**Fig. 14 IDDES centerline plane mean Mach number with velocity streamlines.**

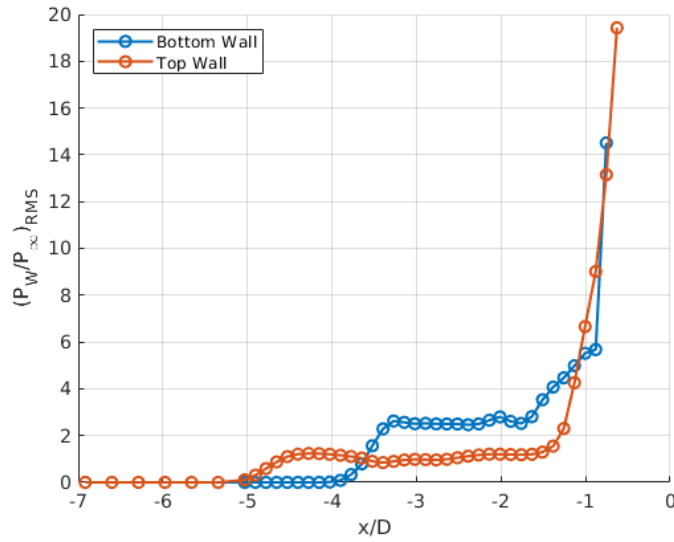**Fig. 15   IDDES pressure centerline top and bottom plate.**

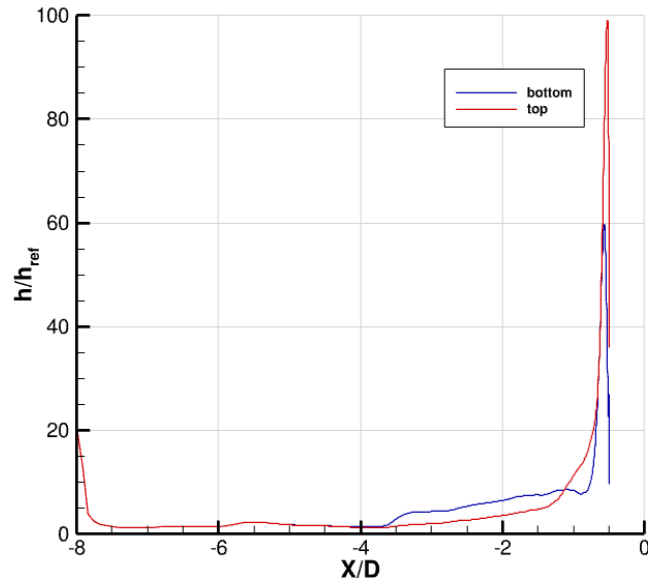**Fig. 16   IDDES pressure RMS fluctuations centerline top and bottom plate.**

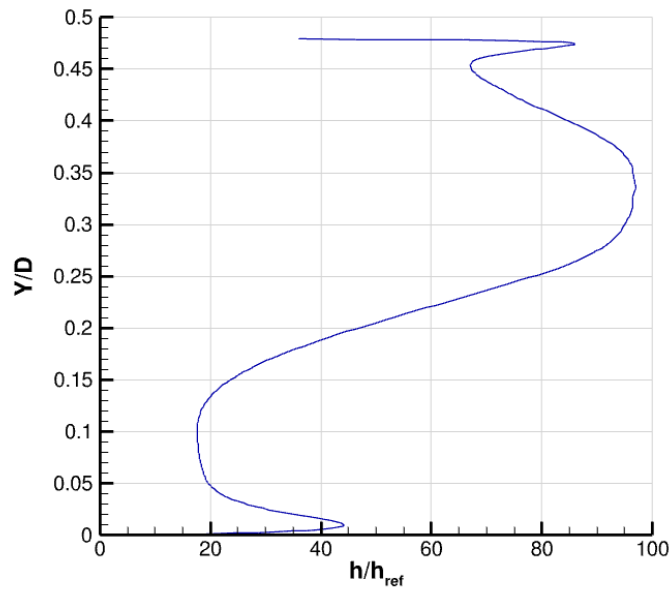**Fig. 17　IDDES heat transfer coefficient centerline top and bottom plate.**

Fig. 18　IDDES heat transfer coefficient cylinder leading edge.

The differences in the general flow structure between the time-averaged IDDES results and the RANS are quite dramatic. The general flow structure, including separation and reattachment points as discussed above, vary between the time-averaged IDDES and the RANS solutions. Additionally, the differences between two instantaneous views of the flow field is quite dramatic due to the large scale motion of the shock system in the streamwise direction. This feature will be discussed more quantitatively using power spectral density. The period of the motion is on the order of 1 millisecond.

The centerplane Mach number contour in Fig. 19 shows the large separation region of low Mach number on the upper surface. A thin area of high Mach number is pushed toward the bottom wall before diverging when reaching the cylinder surface. The streamlines in Fig. 14 show this diverging set of velocity streamlines. The smallest vortex occurs near the top wall junction with the cylinder, the next largest is located at the junction of bottom wall and cylinder, and the largest vortex is upstream of the cylinder on the top wall. Each of these vortices is a location where streamlines are then pushed spanwise out of the path of the cylinder. Figure 20 shows the top wall intersection with the cylinder experiences the highest pressure.

When evaluating the time-averaged IDDES, a moving average was used to evaluate the transient behavior of the start-up of the IDDES simulation. To do this time-series data were collected at points of interest. The heat flux at reattachment on the cylinder, and surface pressure at the separation point on the top wall were selected as metrics of interest. It is recognized that the large scale motion of the flow complicates the time-average, but this was done primarily to evaluate nonphysical transients, and where in the time-history was their influence tolerably small. The moving average of an arbitrary variable ψ is found using the following

$$\psi_{move}(N\Delta t) = \frac{1}{N} \sum_{n=0}^{n=N-1} \psi(n\Delta t) \tag{4}$$

where Δt is time step size, and N is an integer which includes that includes 1 additional time step of the time history at each subsequent point. The moving averages of heat flux on the cylinder and wall pressure at separation are shown in Fig 21 and illustrate the transient behavior. It can be determined that after approximately 3 milliseconds of time, the start-up transients appear be diminishing, and the values asymptote towards their mean value. Additional running would improve results, but computational resources available allowed for the solutions discussed here.
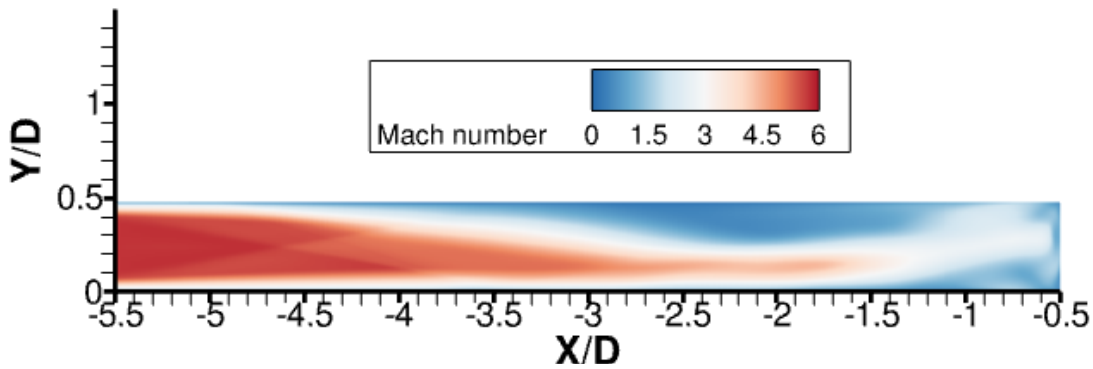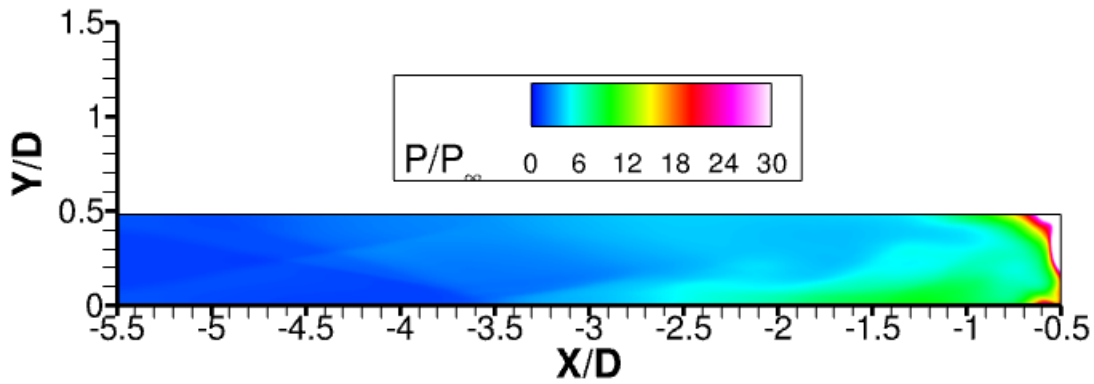

Fig. 19   IDDES centerline plane mean Mach number.

Fig. 20 IDDES centerline plane mean pressure.
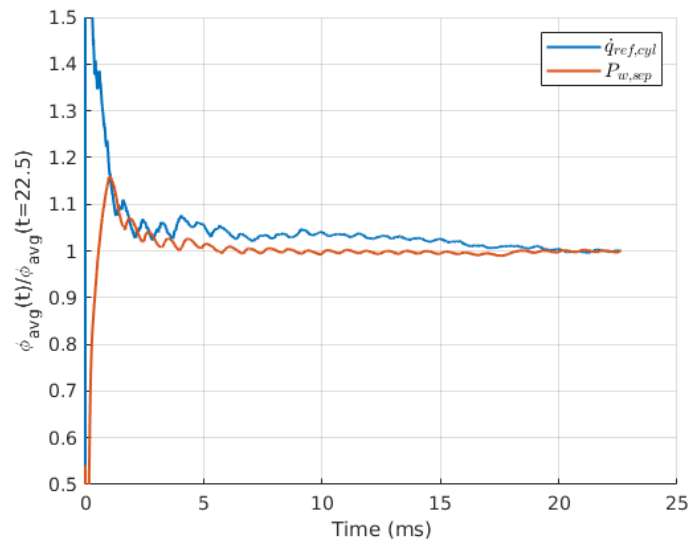

Fig. 21 IDDES moving average of heat flux on the cylinder face, $\dot{q}_w$, and pressure at separation, P_w.

The surfaces in Fig. 22 are colored by the magnitude of skin friction coefficient. The lines on the surfaces are trajectories of the skin friction vector field. Several critical points are called out on the figure to describe the flow patterns [12]. Reattachment streamlines R1 and R2 are both very close to the top and bottom plates. There are two saddle points with a node where the flow reattaches. The reattachment point at N1 is also the location of the peak heating on the cylinder. Separation streamlines: S1 and S2 emanate from the saddle points: SP1 and SP2. The patterns here can also be seen in Fig. 23. In Fig. 24, a separation streamline, S1, can be seen on the top wall. The reattachment line, R1, is very near the cylinder. The gap between the R1 line in the cylinder shows the interaction of the smallest vortex seen in Fig. 14, while the region between R1 and S1 shows the interaction of the largest vortex in the same figure.
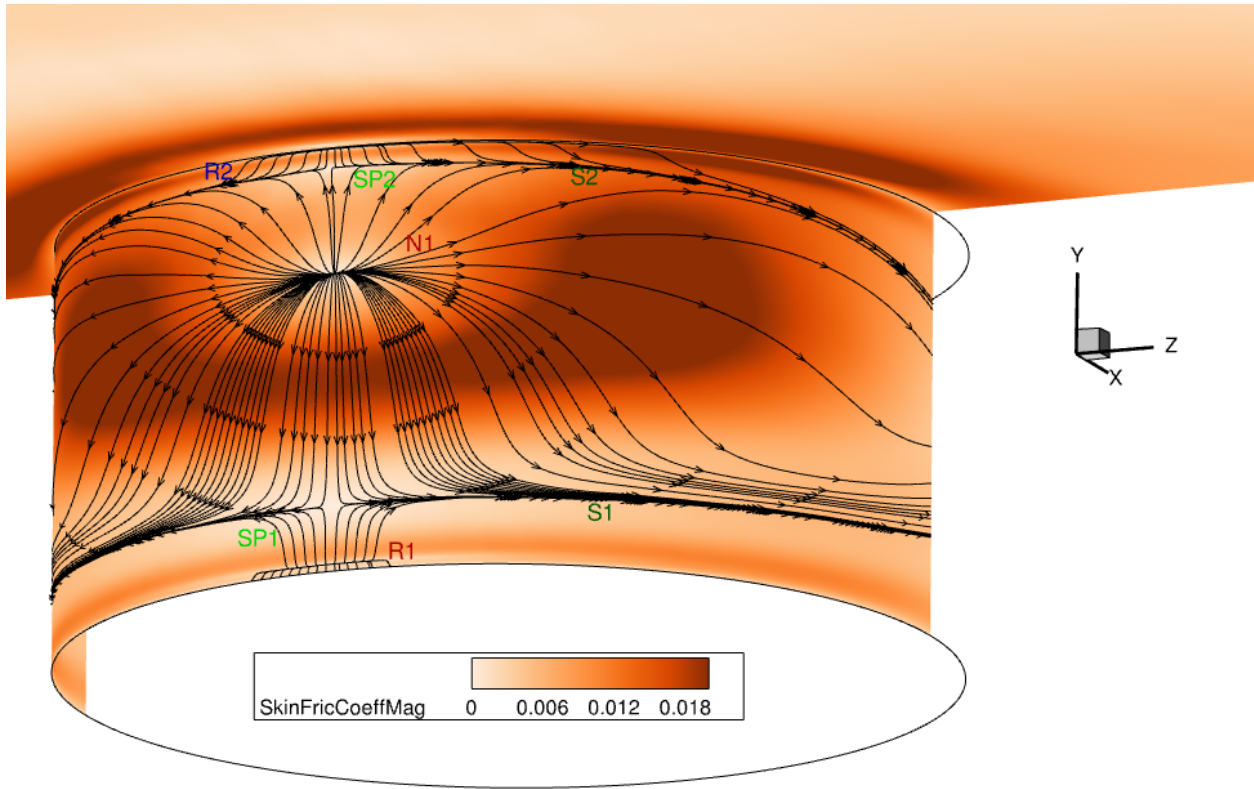
15

Fig. 22   IDDES C_f magnitude contour and skin friction trajectories on upstream cylinder face. Bottom wall and $x/D \geq 0$ are blanked for clarity. Edges of cylinder highlighted for orientation.
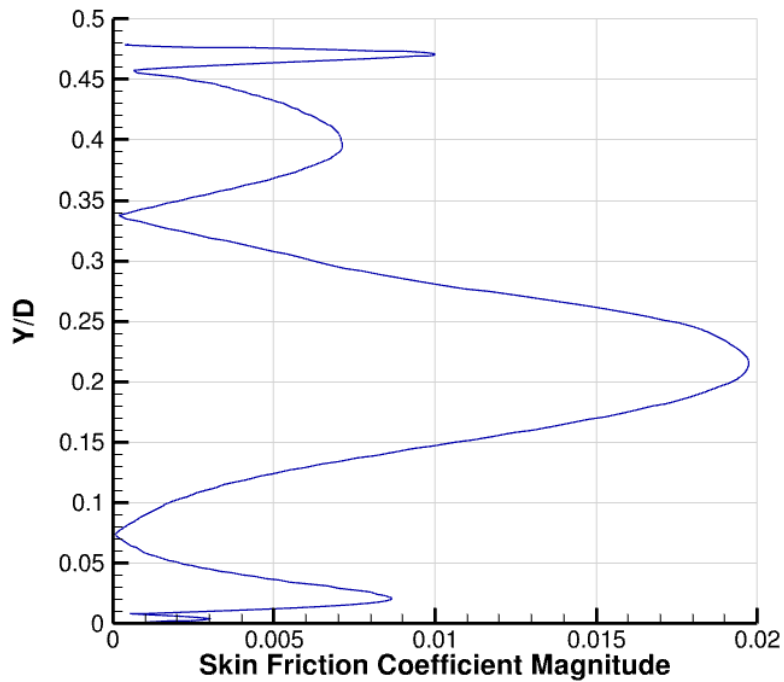

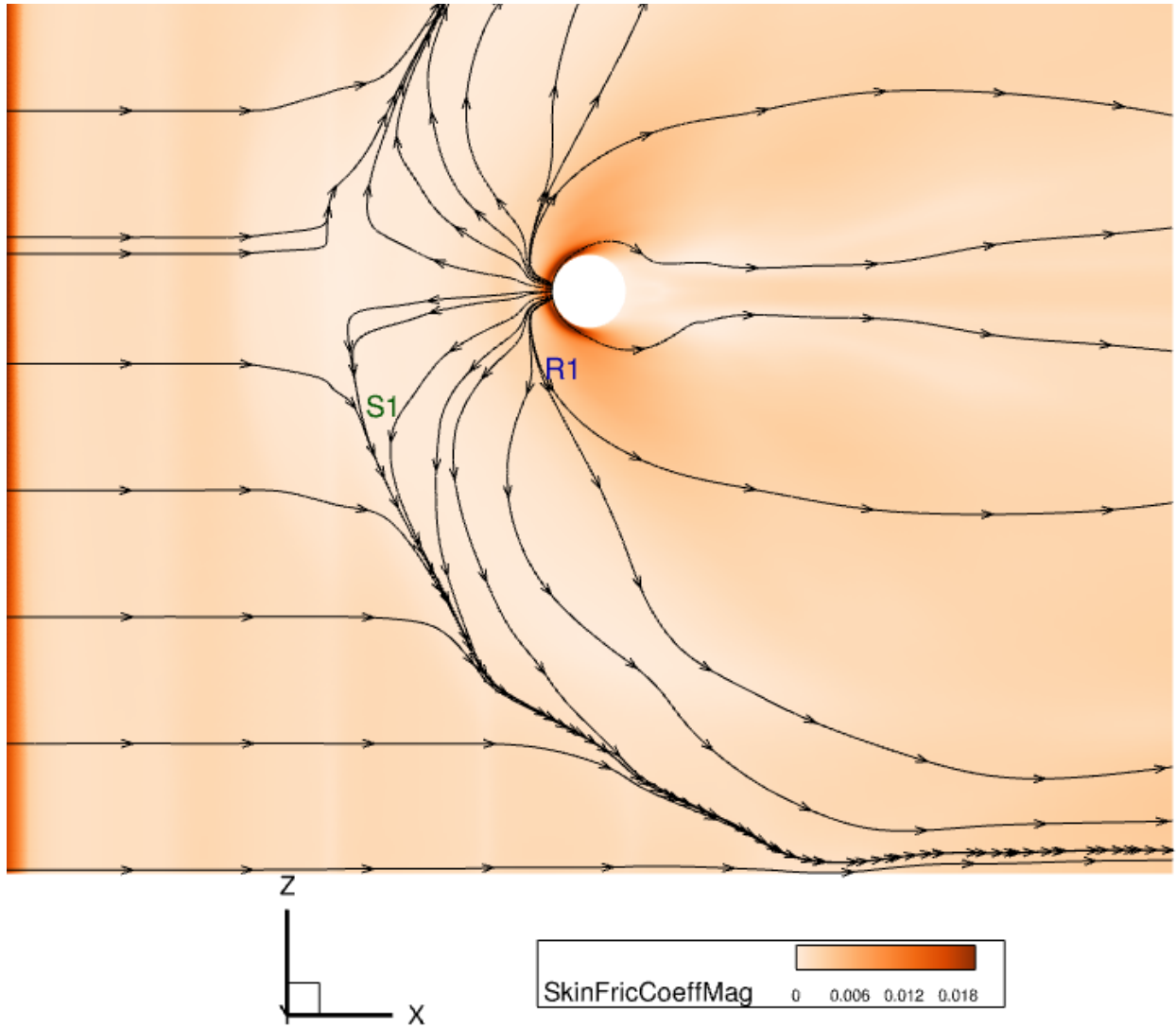**Fig. 23   IDDES C_f magnitude on cylinder on centerline.**

Fig. 24   IDDES C_f magnitude contour and skin friction trajectories on top wall.

Power spectral density analysis of the shock system motion and fluctuating quantities of interest was completed using Welch's method. The power spectral density estimate $G(f)$ was calculated only using the time-history data after the 3 milliseconds past for CFD transients. The sampling frequency $f_s = 10$ MHz for the time-history data used for this analysis corresponds to every computational time step. The time histories were segmented into 8 bins that had 50% overlap and Hamming windowing was used. The spectra are plotted in the conventional premultiplied and normalized form, $fG(f)/\sigma^2$. The function is plotted against the Strouhal number based on cylinder diameter and freestream speed, $St_D = fD/U_\infty$

Premultiplied power spectral density plots of heat flux and surface pressure fluctuations are show in Fig. 25 and Fig. 26. The cylinder separation heat flux fluctuation spectrum corresponds to the SP1 saddle point in Fig. 22. The cylinder reattachment spectrum corresponds to the N1 location on the same figure. The top and bottom wall separation spectrum were taken at the time-averaged separation locations on each wall on the centerline upstream of the cylinder. In Fig. 25 the cylinder separation curve shows a peak power spectral density frequency at $St_D \approx 7$ and relatively little content below $St_D \approx 1$. The cylinder reattachment shows a peak power spectral density frequency at $St_D \approx 2$ with the majority of the content in $1 \leq St_D \leq 10$. Top wall separation has a peak at $St_D \approx 0.1$ with most of its energy content in the intermediate frequencies of $0.1 \leq St_D \leq 1$. The bottom wall separation spectrum has a peak at $St_D \approx 0.02$, but also has a smaller peak near $St_D \approx 1$.

In Fig. 26 the cylinder separation pressure spectrum curve shows a peak power spectral density frequency at $St_D \approx 3$ and again shows relatively little content below $St_D \approx 1$. The cylinder reattachment shows a peak power spectral density frequency at a $St_D \approx 1$ with the content spread widely, $0.1 \leq St_D \leq 10$. Top wall separation has a large peak at $St_D \approx 0.02$ with some content in the range of $0.01 \leq St_D \leq 0.2$. The bottom wall separation spectrum has also a peak at $St_D \approx 0.02$, but also has a smaller peak near $St_D \approx 0.04$ with small amounts of additional content at higher St_D. A Strouhal number peak of roughly 0.03 is often used as characteristic of the location of a shock-wave/boundary-layer interaction separation shock. This agrees with the peaks at low Strouhal number seen in Fig. 25 and Fig. 26. The cylinder separation and reattachment spectrums have much higher frequency content as they represents the impingement dynamics on the cylinder face as opposed to a separating boundary layer. Similar Strouhal number peaks have been documented recently in the blunt-fin work Ngoh and Poggie [11].

Density gradient magnitude contours can be used to distingush shock structures and can give similar insights to experimental schlieren. In the contours in Fig. 27a to Fig. 27k the primary focus is to visualize the unsteadiness within the complex interaction region. The simulation uses IDDES without time varying inflow conditions, and attached boundary layers use the RANS formulation. Beginning at $t = 12$ ms, the reflected oblique shocks from the inflow ($x/D = -8$) can be seen upstream of the separated region. The separation shock originates from the top wall at roughly $x/D = -4.8$. Turbulent structures can be seen in the large recirculation region that forms downstream along the top wall downstream of the separation shock. The separation shock interacts with the bottom wall and reflects. The shocks continue to reflect between the bottom wall and the lower edge of recirculation until the lower wall separates near $x/D = -1.9$. The lower wall vortex can be seen as the turbulent region near the bottom wall downstream of the bottom wall separation location. The complex reflecting shock structure between the two vorticies then reaches the cylinder leading edge. The described structure remains similar in Fig. 27a through Fig. 27e with the primary difference being the locations of the separations on both walls move downstream. By Fig. 27f the furthest location downstream the separations move has occurred and the recirculation region has a higher density gradient and appears to be quite chaotic. The bottom vortex has been pushed to a much smaller region. The compacting of these regions appears to then force the separations back upstream, reestablishing the structure similar to the time-averaged structure. The structures move upstream in Fig 27g through Fig. 27k completing roughly 1 full cycle of motion with a period on the order of 1 millisecond.
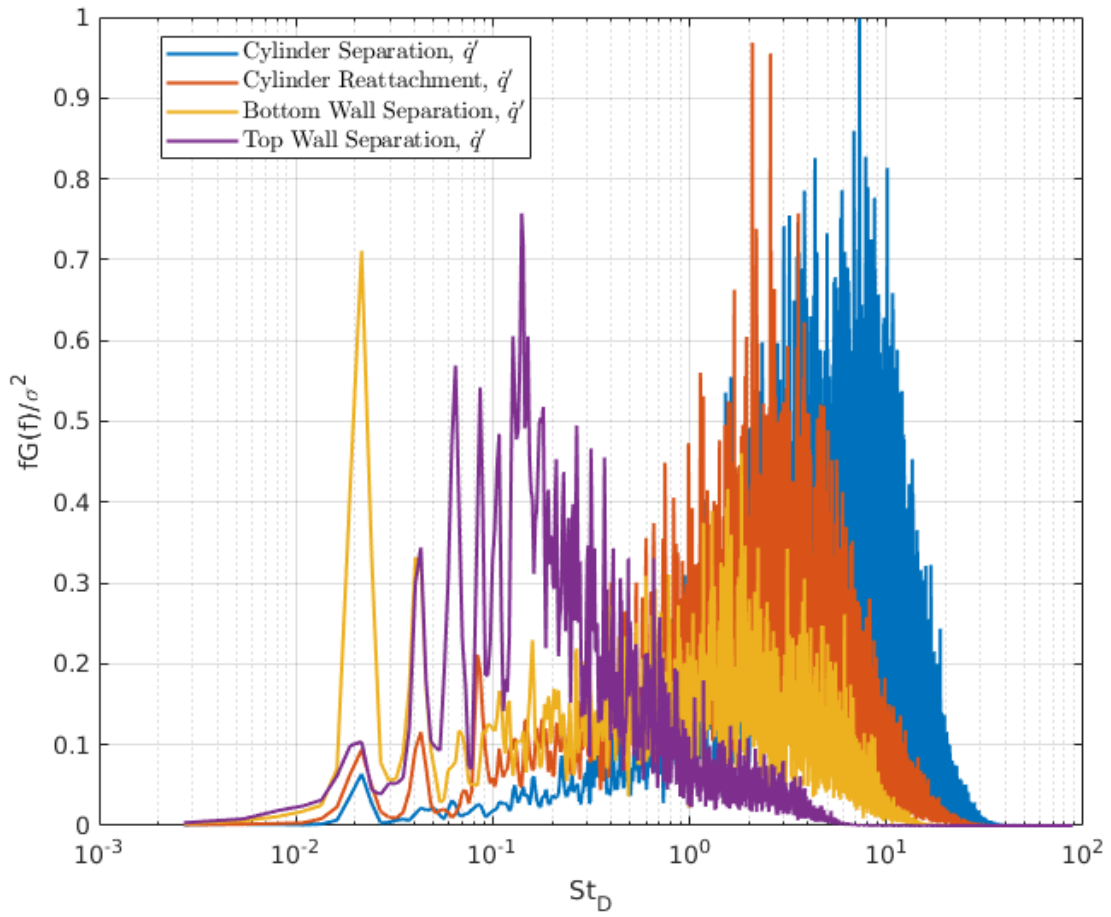
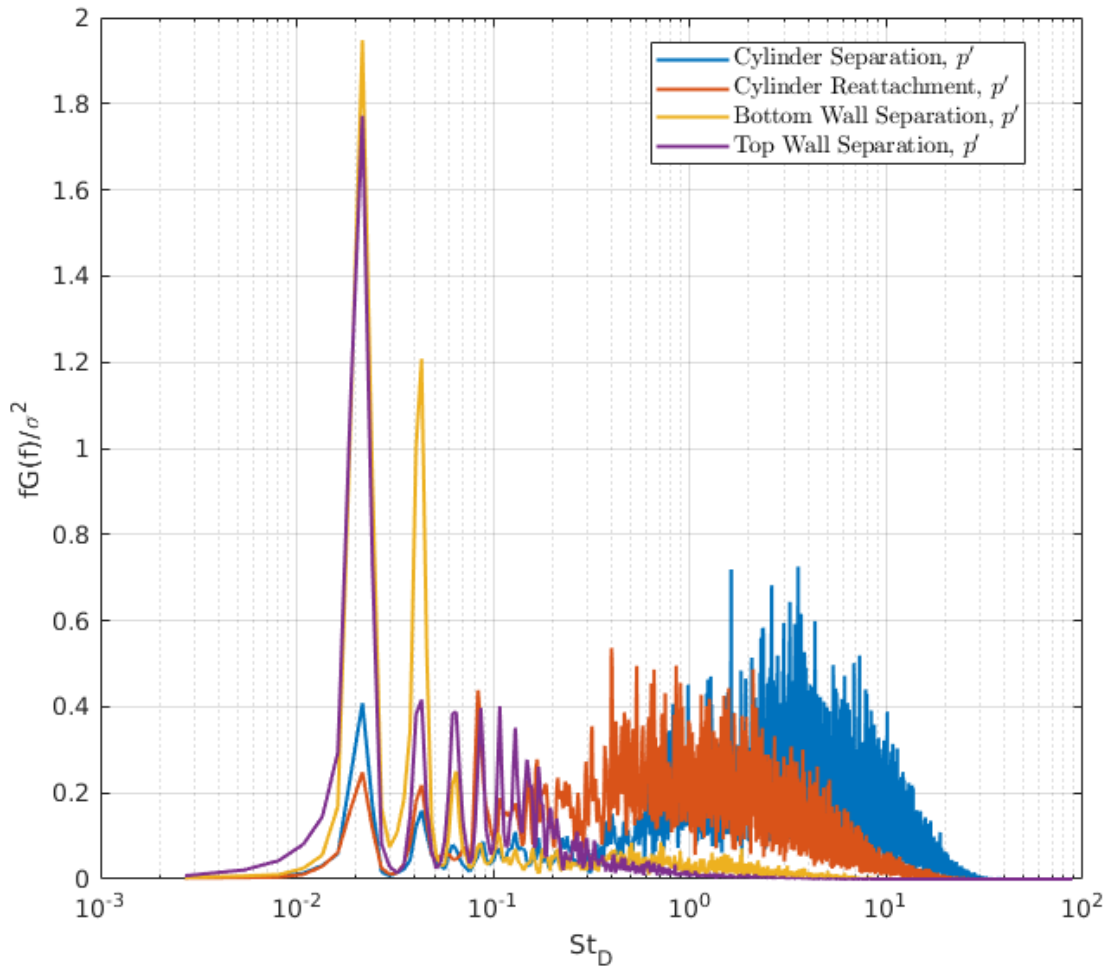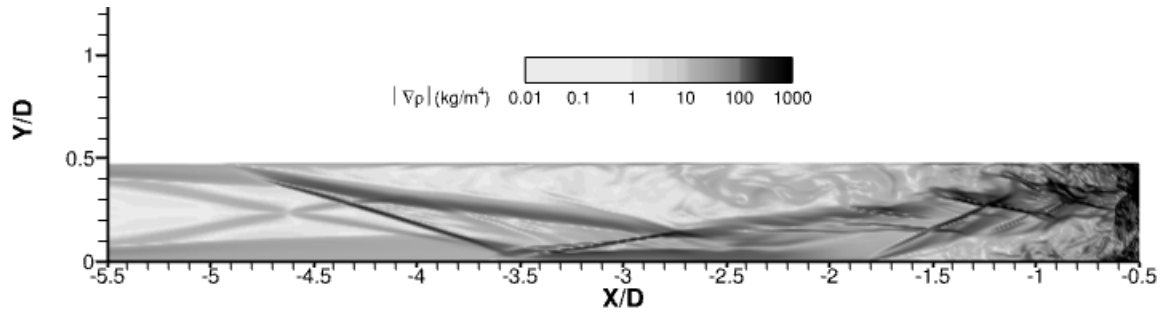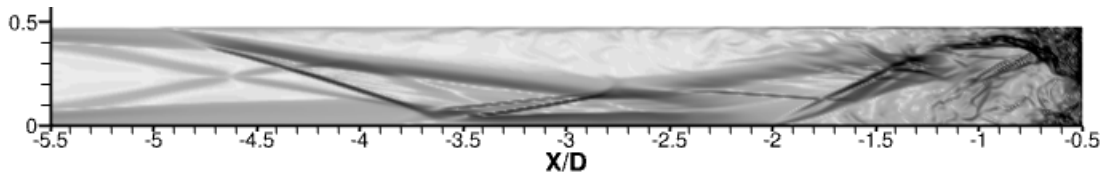**Fig. 25   Centerplane heat flux spectra at select locations.**

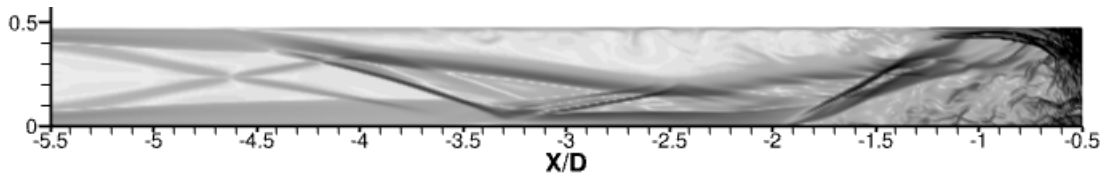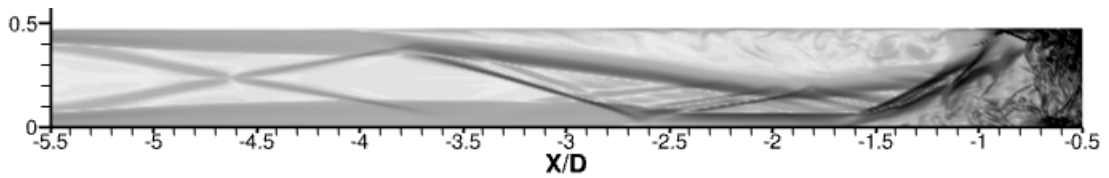**Fig. 26   Centerplane pressure spectra at select locations.**

(a) $t = 12\ ms$
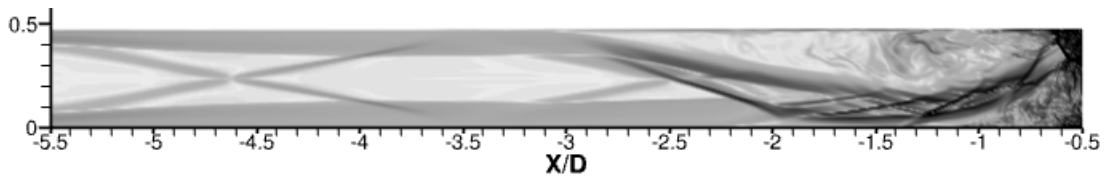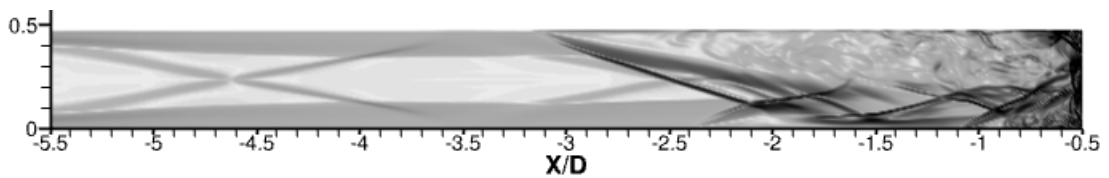
(b) $t = 12.1\ ms$

(c) $t = 12.2\ ms$

(d) $t = 12.3\ ms$

(e) $t = 12.4\ ms$

(f) $t = 12.5\ ms$

Fig. 27 IDDES centerplane instantaneous density gradient magnitude contours.

(g) $t = 12.6 \, ms$

(h) $t = 12.7 \, ms$

(i) $t = 12.8 \, ms$

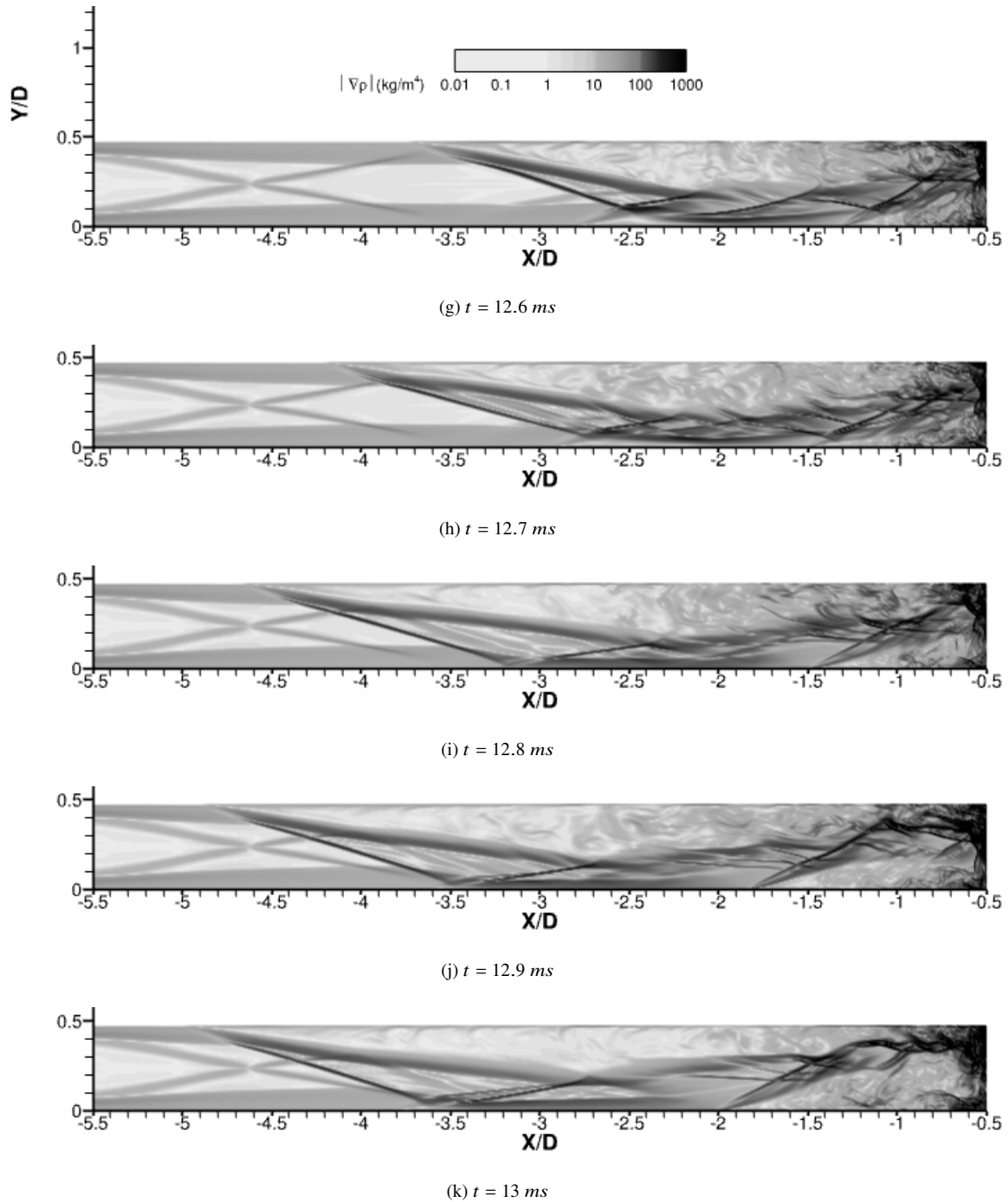(j) $t = 12.9 \, ms$

(k) $t = 13 \, ms$

Fig. 27   IDDES centerplane instantaneous density gradient magnitude contours (Continued).

IV. Conclusion

Reynolds-averaged Navier-Stokes calculations and improved delayed detached eddy simulation were completed for supersonic flow through a configuration consisting of a cylinder located between two flat plates. The flow upstream of the cylinder includes multiple shock-wave/boundary-layer interactions that result in flow separation. Flow visualization was completed to show the flow structure and compare and contrast the RANS and IDDES simulations. The separation locations differed significantly between RANS and IDDES, but similar flow structures were found. The large streamwise

motion of the shock system in the IDDES complicates the analysis when comparing directly to the RANS solution. Time-averaged IDDES simulation contours of Mach number and pressure were compared to RANS. Peak pressures occurred in the IDDES and RANS simulations in the complex flow region near the cylinder junction with one wall. Plots of skin friction, heat transfer coefficient, and surface pressure were compared. RANS and IDDES both predicted extremely high wall pressure and heat transfer on the upstream centerline of the cylinder. Skin friction vector streamlines were used to categorize the flow patterns on the walls and cylinder. Instantaneous solutions were also qualitatively analyzed for the IDDES simulation. Power spectral density analysis was completed for the time-histories from the IDDES. Density gradient magnitude was used to show the large-scale motion of the shock system. The extreme pressure and heating on the walls and cylinder in the flow studied here could cause catastrophic failure if careful consideration of similar geometries are not taken into account when designing a high-speed flight vehicle. The large scale streamwise motion discussed could also cause dramatic fluctuations to the conditions on the surfaces. Continuing to quantify flows in gap regions can help improve the safety and reliability of future high-speed flight.

Acknowledgments

References

[1] Cooper, L., and Putz, K. E., "Generalized Flow in Gaps and Slots Including the Effects of Ablation," *Journal of Spacecraft and Rockets*, Vol. 11, No. 5, 1974, pp. 287–294. https://doi.org/10.2514/3.62065.

[2] Stern, I., and Rowe, W. H., "Effect of gap size on pressure and heating over the flap of a blunt delta wing in hypersonic flow." *Journal of Spacecraft and Rockets*, Vol. 4, No. 1, 1967, pp. 109–114. https://doi.org/10.2514/3.28818.

[3] Clemens, N. T., and Narayanaswamy, V., "Low-Frequency Unsteadiness of Shock Wave/Turbulent Boundary Layer Interactions," *Annual Review of Fluid Mechanics*, Vol. 46, No. 1, 2014, pp. 469–492. https://doi.org/10.1146/annurev-fluid-010313-141346.

[4] Gaitonde, D. V., and Adler, M. C., "Dynamics of Three-Dimensional Shock-Wave/Boundary-Layer Interactions," *Annual Review of Fluid Mechanics*, Vol. 55, No. 1, 2023, pp. 291–321. https://doi.org/10.1146/annurev-fluid-120720-022542.

[5] Neumann, R. D., and Hayes, J. R., "Aerodynamic Heating in the Fin Interaction Region of Generalized Missile Shapes at Mach 6," Tech. Rep. 79-3066, Air Force Flight Dynamics Lab, Wright-Patterson AFB, OH, 1979.

[6] Alviani, R., Fano, D., Poggie, J., and Blaisdell, G., "Aerodynamic Heating in the Gap Between a Missile Body and a Control Fin," *Journal of Spacecraft and Rockets*, Vol. 59, No. 4, 2022, pp. 1111–1124. https://doi.org/10.2514/1.A35183.

[7] Tomaro, R., Strang, W., and Sankar, L., "An implicit algorithm for solving time dependent flows on unstructured grids," *35th Aerospace Sciences Meeting and Exhibit*, 1997. https://doi.org/10.2514/6.1997-333.

[8] Georgiadis, N. J., Rizzetta, D. P., and Fureby, C., "Large-Eddy Simulation: Current Capabilities, Recommended Practices, and Future Research," *AIAA Journal*, Vol. 48, No. 8, 2010, pp. 1772–1784. https://doi.org/10.2514/1.J050232.

[9] Dussauge, J.-P., Dupont, P., and Debiève, J.-F., "Unsteadiness in shock wave boundary layer interactions with separation," *Aerospace Science and Technology*, Vol. 10, No. 2, 2006, pp. 85–91. https://doi.org/https://doi.org/10.1016/j.ast.2005.09.006.

[10] Çengel, Y. A., and Ghajar, A. J., *Heat and Mass Transfer: Fundamentals and Applications*, McGraw-Hill Education, 2014, p. 26.

[11] Ngoh, H., and Poggie, J., "Detached Eddy Simulation of Blunt-Fin-Induced Shock-Wave/Boundary-Layer Interaction," *AIAA Journal*, Vol. 60, No. 4, 2022, pp. 2097–2114. https://doi.org/10.2514/1.J061102.

[12] Délery, J. M., "Robert Legendre and Henri Werlé: Toward the Elucidation of Three-Dimensional Separation," *Annual Review of Fluid Mechanics*, Vol. 33, No. 1, 2001, pp. 129–154. https://doi.org/10.1146/annurev.fluid.33.1.129.